

Axion search with quantum nondemolition detection of magnons

Tomonori Ikeda*

Department of Physics, Kyoto University, Kita-Shirakawa, Sakyo-ku, Kyoto 606-8502, Japan

Asuka Ito†

*Physics Division, National Center for Theoretical Sciences,
National Tsing-Hua University, Hsinchu, 30013, Taiwan*

Kentaro Miuchi,‡ Jiro Soda,§ and Hisaya Kurashige

Department of Physics, Kobe University, Rokkodaicho, Nada-ku, Hyogo 657-8501, Japan

Yutaka Shikano¶

*Quantum Computing Center, Keio University, Hiyoshi,
Kohoku-ku, Yokohama, Kanagawa 223-8522, Japan
Institute for Quantum Studies, Chapman University, CA 92866, USA and
Research Center for Advanced Science and Technology,
The University of Tokyo, Meguro-ku, Tokyo 153-8904, Japan*

(Dated: December 23, 2024)

The axion provides a solution for the strong CP problem and is one of the leading candidates for dark matter. This paper proposes an axion detection scheme based on quantum nondemolition detection of magnon, i.e., quanta of collective spin excitations in solid, which is expected to be excited by the axion–electron interaction predicted by the Dine-Fischer-Srednicki-Zhitnitsky (DFSZ) model. The prototype detector is composed of a ferrimagnetic sphere as an electronic spin target and a superconducting qubit. Both of these are embedded inside a microwave cavity, which leads to a coherent effective interaction between the uniform magnetostatic mode in the ferrimagnetic crystal and the qubit. An upper limit for the coupling constant between an axion and an electron is obtained as $g_{aee} < 1.6 \times 10^{-7}$ at the 95% confidence level for the axion mass of $33.117 \mu\text{eV} < m_a < 33.130 \mu\text{eV}$.

PACS numbers: 95.35.+d, 42.50.Dv

I. INTRODUCTION

The Standard Model successfully predicted the existence of Higgs bosons [1–3]. However, several long-standing problems in particle physics remain to be explained beyond the Standard Model or its alternative. For example, the theory of quantum chromodynamics requires an extremely fine tuning of parameters to explain the experimentally-observed electric dipole moment of the neutron [4, 5]. This issue is considered to be the strong CP problem. To solve this, Peccei and Quinn proposed a global $U(1)$ symmetry that is broken at a high energy scale F_a allowing for the restoration of the CP symmetry, which consequently gives rise to a new pseudoscalar boson called axion [6–8]. Axions can provide a significant fraction of the dark matter (DM) [9]. Therefore, axion DM research is an important field for astrophysics and physics beyond the Standard Model.

The axion model is classified into the Kim-Shifman-Vainshtein-Zakharov (KSVZ) model [10, 11], where ax-

ions couple with photons and hadrons, and the Dine-Fischler-Srednicki-Zhitnitsky (DFSZ) model [12, 13], where axions also couple with electrons [14]. Most experiments for the axion DM research conducted so far were based on the axion–photon coupling through the Primakoff effect [15]. Using this approach, the ADMX experiment excluded the axion mass range of $1.9 \mu\text{eV} < m_a < 3.7 \mu\text{eV}$ for the KVSZ model and $2.66 \mu\text{eV} < m_a < 2.81 \mu\text{eV}$ for the DFSZ model [16]. Alternatively, detection of the axion–electron coupling can provide strong evidence for the DFSZ model. Experiments probing coherent scattering of axions by electrons in the axion mass range of $0.1 \text{ eV} < m_a < 1 \text{ keV}$ were performed [17–19]. This mass range was outside the range of $1 \mu\text{eV} < m_a < 1 \text{ meV}$ favored by the cosmological and astrophysical bounds [20, 21]. An instrument sensitive to the axion–electron coupling in the frequency range of $1 \text{ GHz} < f_a < 1 \text{ THz}$ is required to probe the axion mass in the favorable range, $1 \mu\text{eV} < m_a < 1 \text{ meV}$ as the axion mass and frequency are related by

$$f_a = \frac{\omega_a}{2\pi} = \frac{m_a c^2}{h} \simeq 0.24 \left(\frac{m_a}{1.0 \mu\text{eV}} \right) \text{ GHz}. \quad (1)$$

A possible route that enables probing the axion–electron coupling is based on the detection of quanta of collective spin excitations, called magnons, in a ferrimagnetic crystal [22]. The magnons are to be excited

* ikeda.tomonori.2s@kyoto-u.ac.jp

† aito@cts.nthu.edu.tw

‡ miuchi@phys.sci.kobe-u.ac.jp

§ jiro@phys.sci.kobe-u.ac.jp

¶ yutaka.shikano@keio.jp

through the axion–electron interaction under the strong internal magnetic field inside the crystal. The first experiments based on this axion–electron coupling utilized the hybridization of the uniformly precessing magnetostatic mode, i.e., Kittel mode, in spherical ferrimagnetic crystals and a microwave cavity mode [23–26]. In the experiments they detected an emitted microwave field generated from the magnons that were potentially excited through the axion–electron coupling using a linear receiver [24–26]. An alternative detection method is the magnon counting based on Quantum Non-Demolition (QND) measurements where each measurement does not affect the quantum state of magnons. While linear receivers are ultimately subject to quantum fluctuations, a magnon counting detector is sensitive to the magnon number. Then, the signal-to-noise ratio of the magnon counting detector is only limited by the shot noise on the detected thermal photons, according to Poisson statistics. Especially in Ref. [27], for the case of the axion–photon conversion, it is shown that the photon counting detector can have lower noise than the linear detector under the temperature of 100 mK and the axion and cavity quality factor ratio of $Q_a/Q_c = 20$. Resolving the magnon number was successfully demonstrated by reaching the strong dispersive coupling between a superconducting qubit and the Kittel mode in a spherical ferrimagnetic crystal [28]. In this paper, the data obtained in the setup of Ref. [28] is reanalyzed. In addition, it reports experimental results for axion DM research using a QND detection technique for an axion mass range of $33.117 \mu\text{eV} < m_a < 33.130 \mu\text{eV}$.

II. AXION DETECTION SCHEME

In this section, the theory of axion–electron interaction is first introduced. The axion-induced effective magnetic field generated by the movement of the Earth through axion DM is discussed. After introducing collective spin excitations in a ferrimagnetic crystal, the QND detection scheme of magnons for the axion DM search is described. This is achieved by measuring the absorption spectrum of a superconducting qubit dispersively coupled to the

Kittel mode in the ferrimagnetic crystal.

A. Axion-electron interaction

The axion emerges as a Nambu-Goldstone boson of the broken Peccei-Quinn symmetry [7, 8]. In the DFSZ model [14], the axion field $a(x)$ can interact with an electron field $\psi(x)$ as

$$\mathcal{L}_{\text{int}} = -ig_{aee}a(x)\bar{\psi}(x)\gamma_5\psi(x), \quad (2)$$

where g_{aee} is a dimensionless coupling constant, inversely proportional to the energy scale of the Peccei-Quinn symmetry breaking. Note that we can rewrite the interaction of Eq. (2) as $\tilde{g}_{aee}(\partial_\mu a)\bar{\psi}\gamma^\mu\gamma_5\psi(x)$ using the background Dirac equation, where $\tilde{g}_{aee} = g_{aee}/2m_e$. This clearly shows the shift symmetry of the axion field. In the non-relativistic limit, the interaction term reads

$$\mathcal{H}_{\text{int}} \simeq -\frac{g_{aee}\hbar}{2m_e}\hat{\boldsymbol{\sigma}} \cdot \nabla a = -2\mu_B\hat{\mathbf{S}} \cdot \left(\frac{g_{aee}}{e}\nabla a\right), \quad (3)$$

where m_e is the electron mass, e is the elementary electric charge, $\mu_B = e\hbar/2m_e$ is the Bohr magneton. The electron spin operator $\hat{\mathbf{S}}$ is related to the Pauli matrices $\hat{\boldsymbol{\sigma}}$ with $\hat{\mathbf{S}} = \hat{\boldsymbol{\sigma}}/2$. The term in the parentheses can be considered as an effective magnetic field

$$\mathbf{B}_a = \frac{g_{aee}}{e}\nabla a. \quad (4)$$

If the DM is composed of axions, this effective magnetic field is ubiquitous around us. Importantly, the axion DM is oscillating in time at the frequency f_a that is related to its mass according to Eq. (1).

B. Axion-induced effective magnetic field

It is assumed that the axion DM forms solitonic objects, oscillating coherently with the frequency (1) inside of them [29, 30]. The radius of such axion clumps, namely the Jeans length r_{ob} , can be estimated by applying the virial theorem to the object. This is based on the assumption that the Jeans length is roughly equal to the de Broglie wavelength of the axion. This leads to

$$r_{\text{ob}} \sim 6.8 \times 10^{11} \left(\frac{1.0 \mu\text{eV}}{m_a}\right)^{1/2} \left(\frac{0.45 \text{ GeV/cm}^3}{\rho_{\text{ob}}}\right)^{1/4} \text{ m}, \quad (5)$$

where ρ_{ob} is the energy density of the object. Here, $\rho_{\text{ob}} = 0.45 \text{ GeV/cm}^3$ is assumed to be the local DM density, although it could be several orders of magnitude higher. As the objects are moving with the virial velocity v in the Galaxy (see Appendix. A for detail), where the coherence time is estimated as

$$t_{\text{ob}} \sim \frac{r_{\text{ob}}}{v} \simeq 2.3 \times 10^6 \times \left(\frac{1.0 \mu\text{eV}}{m_a}\right)^{1/2} \left(\frac{0.45 \text{ GeV/cm}^3}{\rho_{\text{ob}}}\right)^{1/4} \left(\frac{300 \text{ km/s}}{v}\right) \text{ s}. \quad (6)$$

Notably, the coherence time, during which the effective magnetic field is coherent, is considered to be much longer than the observation time for the present experiment.

For the coherently oscillating object, it is expected that the distribution of the axion field is almost homogeneous due to the uncertainty principle. In particular, the axion field cannot vary in the length scale smaller than its de

Broglie wavelength. Even then, the spatial gradient of the axion field is nonzero, as the object is moving with the velocity v relative to the laboratory frame [31]. We then have a relation $\partial_i a \simeq m_a v a$ because the proper time of the moving object depends on the coordinates of our frame through the Lorentz transformation. The amplitude of the effective magnetic field B_a can be estimated from Eq. (4) and the relation $\rho_{\text{ob}} \sim m_a^2 a^2 / 2$, resulting in

$$B_a \simeq 4.4 \times 10^{-8} \times g_{aee} \left(\frac{\rho_{\text{ob}}}{0.45 \text{ GeV/cm}^3} \right)^{1/2} \left(\frac{v}{300 \text{ km/s}} \right) \text{ T.} \quad (7)$$

The amplitude is negligible if we consider the astrophysics constraint of $g_{aee} \lesssim 10^{-12}$ from the bounds on the cooling of white dwarfs [32]. However, as demonstrated later, the coupling constant can effectively be enhanced for collective spin excitation modes in ferrimagnetic crystals.

C. Collective spin excitations

Let us consider a ferrimagnetic crystal containing N electron spins. This system is described by the Heisenberg model [33]

$$\hat{\mathcal{H}}_{\text{m-a}} = g\mu_B \sum_i \hat{\mathbf{S}}_i \cdot (\mathbf{B}_0 + \mathbf{B}_a) - \sum_{i,j} J_{ij} \hat{\mathbf{S}}_i \cdot \hat{\mathbf{S}}_j, \quad (8)$$

where, \mathbf{B}_0 is the external magnetic field, g is the g -factor for electron spins in the ferrimagnetic crystal, and i labels each spins. The second term represents the exchange interaction between the neighboring spins with the strength J_{ij} . Considering an external magnetic field \mathbf{B}_0 along the z -axis and assuming, without loss of generality, that the direction of the effective magnetic field \mathbf{B}_a ($B_a \ll B_0$) lies in the z - x plane, we write

$$\mathbf{B}_0 = (0, 0, B_0), \quad \mathbf{B}_a \simeq (|\mathbf{B}_a| \sin \theta, 0, 0). \quad (9)$$

Here, θ is the angle between the external and effective magnetic fields.

The effective magnetic field is considered to be uniform throughout the sample during the typical observation time. Thus, the effective magnetic field can be written as

$$\mathbf{B}_a(t) = \frac{B_a \sin \theta}{2} (e^{-i\omega_a t} + e^{i\omega_a t}) (1, 0, 0). \quad (10)$$

Substituting Eqs. (9) and (10) into Eq. (8) yields

$$\begin{aligned} \hat{\mathcal{H}}_{\text{m-a}} = & g\mu_B \sum_i \left[\hat{S}_i^z B_0 + \frac{B_a \sin \theta}{4} (\hat{S}_i^- e^{-i\omega_a t} + \hat{S}_i^+ e^{i\omega_a t}) \right] \\ & - \sum_{i,j} J_{ij} \hat{\mathbf{S}}_i \cdot \hat{\mathbf{S}}_j, \end{aligned} \quad (11)$$

where $S_j^\pm = S_j^x \pm iS_j^y$ are the spin ladder operators. The second term in the right-hand side of Eq. (11) shows that the axion DM excites the spins if the frequency of the effective magnetic field ω_a is equal to the Larmor frequency $\omega_m \equiv g\mu_B B_0 / \hbar$.

The spin system of Eq. (11), including the axion-induced effective magnetic field, can be rewritten in terms of the bosonic operators \hat{C}_i and \hat{C}_i^\dagger , which satisfies the commutation relation $[\hat{C}_i, \hat{C}_j^\dagger] = \delta_{ij}$, using the Holstein-Primakoff transformation [34]:

$$\begin{aligned} \hat{S}_i^z &= \frac{1}{2} - \hat{C}_i^\dagger \hat{C}_i, \\ \hat{S}_i^+ &= \sqrt{1 - \hat{C}_i^\dagger \hat{C}_i} \hat{C}_i, \\ \hat{S}_i^- &= \hat{C}_i^\dagger \sqrt{1 - \hat{C}_i^\dagger \hat{C}_i}. \end{aligned} \quad (12)$$

This introduces spin waves with a dispersion relation determined by the amplitude of the external magnetic field B_0 and the amplitudes J_{ij} of the ferrimagnetic exchange interaction. Magnons are quanta of the spin-wave modes. Furthermore, provided that the contributions from the surface of the sample are negligible, one can expand the bosonic operators in terms of plane waves as follows:

$$\hat{C}_i = \frac{1}{\sqrt{N}} \sum_{\mathbf{k}} e^{-i\mathbf{k} \cdot \mathbf{r}_i} \hat{c}_{\mathbf{k}}. \quad (13)$$

Here, \mathbf{r}_i is the position vector of spin i , and $\hat{c}_{\mathbf{k}}$ annihilates a magnon from the mode with a wave vector \mathbf{k} . As the effective magnetic field is induced by axions, it is supposed to be homogeneous over the ferrimagnetic crystal for a typical experiment. Then, only the uniform magnetostatic mode, Kittel mode, can be excited as long as the contributions from the surface are negligible [35]. Substituting Eqs. (12) and (13) into the Hamiltonian of

Eq. (11) yields

$$\hat{\mathcal{H}}_{m-a} \equiv \hat{\mathcal{H}}_m + \hat{\mathcal{H}}_a, \quad (14)$$

$$\hat{\mathcal{H}}_m = \hbar\omega_m \hat{c}^\dagger \hat{c}, \quad (15)$$

$$\hat{\mathcal{H}}_a = g\mu_B \frac{B_a \sin \theta}{4} \sqrt{N} (\hat{c}^\dagger e^{-i\omega_a t} + \hat{c} e^{i\omega_a t}), \quad (16)$$

where $\hat{c} \equiv \hat{c}_{k=0}$ and $\bar{n}_m \equiv \langle \hat{c}^\dagger \hat{c} \rangle \ll N$ are assumed. One can see that the coupling strength is enhanced by a factor of \sqrt{N} . This effect enables one to potentially detect the small effective magnetic field B_a oscillating at ω_a .

D. Quantum nondemolition detection of magnons

To detect the excitation of a magnon in the Kittel mode, a hybrid system schematically shown in Fig. 1 is used. This system consists of a spherical ferrimagnetic crystal and a superconducting qubit [36]. They are individually coupled to the modes of a microwave cavity through magnetic and electric dipole interactions, respectively. This leads to an effective coherent coupling between the Kittel mode and the qubit [28, 37–40]. The transmon-type superconducting qubit [41] can be described as an anharmonic oscillator through the Hamiltonian

$$\hat{\mathcal{H}}_q/\hbar = \left(\omega_q - \frac{\alpha}{2}\right) \hat{q}^\dagger \hat{q} + \frac{\alpha}{2} (\hat{q}^\dagger \hat{q})^2, \quad (17)$$

where ω_q is the frequency of the transition between the ground and first-excited states of the qubit, $|g\rangle$ and $|e\rangle$, respectively. The creation and annihilation operators for the qubit are respectively \hat{q}^\dagger and \hat{q} . Furthermore, the anharmonicity $\alpha < 0$ of the qubit is defined such that the frequency of the transition between the first and second excited states is given by $\omega_q + \alpha$ [42]. After adiabatically eliminating the microwave cavity modes from the total Hamiltonian of the hybrid system, the effective interaction Hamiltonian between the Kittel mode and the qubit is given by

$$\hat{\mathcal{H}}_{q-m}/\hbar = g_{q-m} (\hat{q}^\dagger \hat{c} + \hat{q} \hat{c}^\dagger), \quad (18)$$

where g_{q-m} is the coupling strength between the Kittel mode and the qubit [28, 37–39].

Combining Eqs. (14), (17) and (18), the Hamiltonian of the hybrid quantum system, including the effective axion-induced effective magnetic field, is given by:

$$\begin{aligned} \hat{\mathcal{H}}_{\text{tot}}/\hbar = & \omega_m \hat{c}^\dagger \hat{c} + \left(\omega_q - \frac{\alpha}{2}\right) \hat{q}^\dagger \hat{q} + \frac{\alpha}{2} (\hat{q}^\dagger \hat{q})^2 \\ & + g_{q-m} (\hat{q}^\dagger \hat{c} + \hat{q} \hat{c}^\dagger) + g_{\text{eff}} (\hat{c}^\dagger e^{-i\omega_a t} + \hat{c} e^{i\omega_a t}). \end{aligned} \quad (19)$$

Here,

$$\hbar g_{\text{eff}} = g\mu_B \frac{B_a \sin \theta}{4} \sqrt{N}, \quad (20)$$

is the effective coupling constant between axions and magnons, which corresponds to the strength of the coherent magnon drive.

Let us consider the dispersive regime corresponding to a detuning $\Delta_{q-m} \equiv \omega_q - \omega_m$ between the qubit frequency ω_q and the frequency of the Kittel mode ω_m . That is much larger than the coupling strength g_{q-m} such that the exchange of energy between the two systems is highly suppressed [28]. For this limit, the total Hamiltonian of Eq. (19) can be rewritten as

$$\begin{aligned} \hat{\mathcal{H}}'_{\text{tot}}/\hbar \simeq & \omega_m \hat{c}^\dagger \hat{c} + \frac{1}{2} \tilde{\omega}_q \hat{\sigma}_z + \chi_{q-m} \hat{c}^\dagger \hat{c} \hat{\sigma}_z \\ & + g_{\text{eff}} (\hat{c}^\dagger e^{-i\omega_a t} + \hat{c} e^{i\omega_a t}), \end{aligned} \quad (21)$$

where $\tilde{\omega}_q = \omega_q + \chi_{q-m}$ is the qubit frequency shifted by the qubit-magnon dispersive shift χ_{q-m} , which is described by [42].

$$\chi_{q-m} \simeq \frac{\alpha g_{q-m}^2}{\Delta_{q-m} (\Delta_{q-m} + \alpha)}. \quad (22)$$

The qubit-magnon dispersive shift can also be estimated numerically by diagonalizing the Hamiltonian of the hybrid system [28]. The Hamiltonian of Eq. (21) considers only the first two states of the qubit through the Pauli matrices: $\hat{\sigma}_z = |e\rangle\langle e| - |g\rangle\langle g|$, $\hat{\sigma}_+ = |e\rangle\langle g|$, and $\hat{\sigma}_- = |g\rangle\langle e|$. Furthermore, higher order terms in (g_{q-m}/Δ_{q-m}) are neglected. The third term on the right-hand side of Eq. (21) shows that the qubit frequency depends on the magnon occupancy through an interaction term, which commutes with the Hamiltonian of the Kittel mode. More specifically, the qubit frequency $\tilde{\omega}_q$ shifts by $2\chi_{q-m}$ for every magnon in the Kittel mode. Therefore, measuring the qubit frequency enables one to perform a QND detection for the magnon number.

E. Qubit spectrum

The qubit frequency can be determined, for example, by measuring its absorption spectrum

$$S(\omega_s) = \text{Re} \left[\frac{1}{\sqrt{2\pi}} \int_0^\infty dt \langle \hat{\sigma}_-(t) \hat{\sigma}_+(0) \rangle e^{i\omega_s t} \right], \quad (23)$$

where ω_s is the spectroscopy frequency [42]. In this subsection, an analytical model for the qubit spectrum in the presence of a dispersive interaction with the Kittel mode of a ferrimagnetic crystal is provided [28, 42]. For this purpose, the Hamiltonian of Eq. (21) is transformed such that the qubit is in a reference frame that rotates at the spectroscopy frequency ω_s . Meanwhile, the Kittel mode is in a reference frame that rotates at the axion frequency ω_a . The Hamiltonian of Eq. (21) becomes

$$\begin{aligned} \hat{\mathcal{H}}/\hbar = & (\Delta_a + \chi_{q-m}) \hat{c}^\dagger \hat{c} + \frac{1}{2} \Delta_s \hat{\sigma}_z + \chi_{q-m} \hat{c}^\dagger \hat{c} \hat{\sigma}_z \\ & + g_{\text{eff}} (\hat{c}^\dagger + \hat{c}) + \Omega_s (\hat{\sigma}_+ + \hat{\sigma}_-), \end{aligned} \quad (24)$$

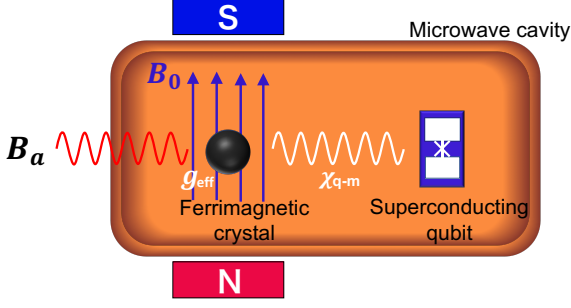


FIG. 1. Schematic illustration of the detector. A spherical ferrimagnetic crystal and a transmon-type superconducting qubit are coherently coupled through a microwave cavity. The effective magnetic field of the axion DM coherently drives the uniform spin-precession mode (Kittel mode) in the ferrimagnetic crystal with an effective coupling constant g_{eff} . In the strong dispersive regime, each magnon excited in the Kittel mode shifts the resonance frequency of the qubit by $2\chi_{q-m} + \Delta_a$, where χ_{q-m} is the dispersive shift and $\Delta_a = \omega_m^g - \omega_a$ is the detuning between the frequency ω_a of the axion-induced effective magnetic field and the frequency ω_m^g of the Kittel mode with the qubit in the ground state $|g\rangle$.

where $\Delta_a = \omega_m^g - \omega_a$ is the detuning between the frequency ω_m^g of the Kittel mode with the qubit in the ground state $|g\rangle$ and the axion frequency ω_a . In addition, $\Delta_s = \tilde{\omega}_q - \omega_s$ is the detuning between the frequency $\tilde{\omega}_q$ of the qubit and the spectroscopy frequency ω_s . The amplitudes of the driving terms are given by the effective coupling constant g_{eff} and the Rabi frequency Ω_s , respectively. When considering the decoherences for the Kittel mode and the qubit that are characterized by linewidths γ_m and γ_q , respectively, the qubit spectrum is given by [42]

$$S(\omega_s) = \frac{1}{\pi} \sum_{n_m=0}^{\infty} \frac{1}{n_m!} \text{Re} \left[\frac{(-A)^{n_m} e^A}{\gamma_q^{(n_m)}/2 - i(\omega_s - \tilde{\omega}_q^{(n_m)})} \right], \quad (25)$$

with

$$\omega_q^{(n_m)} = \tilde{\omega}_q + B + 2\chi_{q-m}n_m, \quad (26)$$

$$\tilde{\omega}_q^{(n_m)} = \omega_q^{(n_m)} + n_m\Delta_a, \quad (27)$$

$$\gamma_q^{(n_m)} = \gamma_q + \gamma_m(n_m + D^{\text{ss}}), \quad (28)$$

$$A = D^{\text{ss}} \left(\frac{\gamma_m/2 - i(\Delta_a + 2\chi_{q-m})}{\gamma_m/2 + i(\Delta_a + 2\chi_{q-m})} \right), \quad (29)$$

$$B = \chi_{q-m}(\bar{n}_m^g + \bar{n}_m^e - D^{\text{ss}}), \quad (30)$$

$$D^{\text{ss}} = \frac{2(\bar{n}_m^g + \bar{n}_m^e)\chi_{q-m}^2}{(\gamma_m/2)^2 + \chi_{q-m}^2 + (\chi_{q-m} + \Delta_a)^2}, \quad (31)$$

$$\bar{n}_m^g = \frac{g_{\text{eff}}^2}{(\gamma_m/2)^2 + \Delta_a^2}, \quad (32)$$

$$\bar{n}_m^e = \frac{g_{\text{eff}}^2}{(\gamma_m/2)^2 + (\Delta_a + 2\chi_{q-m})^2}. \quad (33)$$

Here, $\tilde{\omega}_q^{(n_m)}$ and $\gamma_q^{(n_m)}$ are respectively the frequency and the linewidth of the qubit with the Kittel mode in the number state $|n_m\rangle$ for a given effective coupling constant g_{eff} . Equations (31) [(32)] expresses the steady-state magnon occupancy when the qubit is in the ground (excited) state, which is given by $\bar{n}_m^{g(e)}$.

In the strong dispersive regime, which corresponds to $2\chi_{q-m} \gg \gamma_m$, the qubit spectrum is given by a sum of Lorentzian functions centered at the shifted qubit frequency $\tilde{\omega}_q^{(n_m)}$. The spectrum explicitly depends on the population of the magnons potentially excited by the axion-induced effective magnetic field B_a . Therefore, the axion DM can be probed by measuring the spectrum of the qubit that is coupled to the Kittel mode in the ferrimagnetic crystal.

Figure 2 shows the expected qubit spectrum for the different values of the coupling constant g_{aee} considering a spherical ferrimagnetic crystal of yttrium iron garnet ($\text{Y}_3\text{Fe}_5\text{O}_{12}$, YIG). This crystal is considered to have a diameter of 0.5 mm with a net spin density of $\sim 2.1 \times 10^{22} \text{ cm}^{-3}$ and the following realistic parameters: $\omega_m^g/2\pi = 8.0 \text{ GHz}$, $\omega_a/2\pi = 8.0 \text{ GHz}$ (corresponding to an axion mass $m_a \approx 33 \mu\text{eV}$), $\tilde{\omega}_q/2\pi = 8.2 \text{ GHz}$, $\gamma_m/2\pi = 1.0 \text{ MHz}$, $\gamma_q/2\pi = 0.1 \text{ MHz}$, and $\chi_{q-m}/2\pi = 10 \text{ MHz}$. For the calculation, the magnon number is truncated at $n_m = 10$, which is justified for $\bar{n}_m^{g(e)} \ll 1$. Without the axion-induced magnetic field ($g_{aee} = 0$), only one peak appears at the qubit frequency $\tilde{\omega}_q^{(0)} = \tilde{\omega}_q$. On the other hand, for $g_{aee} = 5.0 \times 10^{-7}$, a second peak at $\tilde{\omega}_q^{(1)} \approx \tilde{\omega}_q^{(0)} + 2\chi_{q-m}$ appears. This second peak corresponds to the excitation of a single magnon in the Kittel mode due to the axion DM. Therefore, the observation of a peak around the frequency $\tilde{\omega}_q^{(1)}$ demonstrates the existence of the axion DM.

III. EXPERIMENT

In Ref. [28], owing to the strong dispersive regime between the uniform magnetostatic mode of the spherical ferrimagnetic crystal and a superconducting qubit, quanta of the collective spin excitations were observed under an additional resonant drive of the Kittel mode. Here, the data without an intentional drive is analyzed for the search of axion DM. More details about the experiment can be found in Ref. [28].

A. Device and parameters

As depicted in Fig. 1, the hybrid quantum system consists of a superconducting qubit and a single crystalline sphere of YIG, both inside a three-dimensional microwave cavity. The diameter of the YIG sphere is 0.5 mm. A pair of permanent magnets and a coil are used to apply an external magnetic field $B_0 \approx 0.29 \text{ T}$

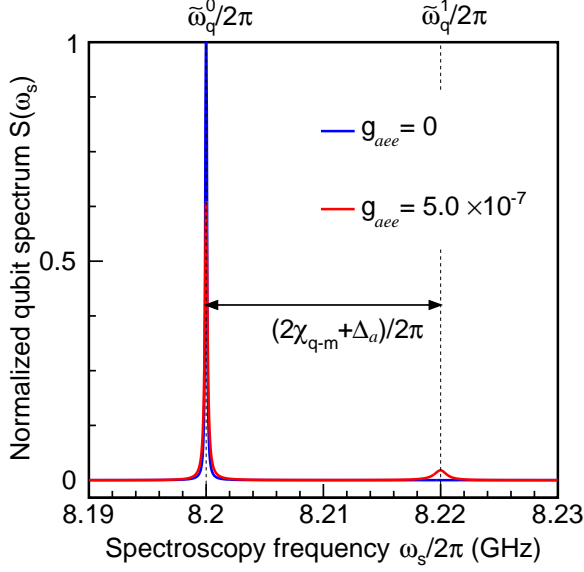


FIG. 2. Normalized qubit spectra $S(\omega_s)$ in the absence and presence of a coupling with axions, shown as the blue ($g_{aee} = 0$) and red ($g_{aee} = 5.0 \times 10^{-7}$) lines, respectively. The parameters used here are $\omega_m^g/2\pi = 8.0$ GHz, $\omega_a/2\pi = 8.0$ GHz, $\tilde{\omega}_q/2\pi = 8.2$ GHz, $\gamma_m/2\pi = 1.0$ MHz, $\gamma_q/2\pi = 0.1$ MHz, and $\chi_{q-m}/2\pi = 10$ MHz.

for the YIG sphere. The transmon-type superconducting qubit has a frequency $\tilde{\omega}_q/2\pi \approx 7.99$ GHz.

The superconducting qubit and the Kittel mode of the ferrimagnetic crystal are coherently coupled by their individual interactions with the modes of the microwave cavity [28, 37, 38]. The effective coupling strength $g_{q-m}/2\pi = 7.79$ MHz is experimentally determined from the magnon-vacuum Rabi splitting of the qubit. This coupling strength is much larger than the power-broadened qubit linewidth γ_q and the magnon linewidth γ_m [28].

The frequency of the Kittel mode is set based on the current in the coil to reach the dispersive regime of the interaction between the uniform mode and the qubit. The amplitude of the detuning $|\Delta_{q-m}| = |\tilde{\omega}_q - \omega_m^g|$ is much larger than the coupling strength g_{q-m} . The qubit-magnon dispersive shift $\chi_{q-m}/2\pi = 1.5 \pm 0.1$ MHz and the dressed magnon frequency $\omega_m^g/2\pi = 7.94962$ GHz are obtained. These values are summarized in Table I.

B. Measurements and results

Here we analyze the qubit spectrum obtained in the experiment of Ref. [28] without an intentional excitation of the Kittel mode. The qubit absorption spectrum shown in Fig. 3 was measured in the frequency range $7.9825 \text{ GHz} < \omega_s/2\pi < 8.0025 \text{ GHz}$ with a resolution of 100 kHz. The measurement lasted approximately 4 hours

and each bin of 50 measurements was averaged.

The measured spectrum is fitted according to the following equation,

$$\tilde{S}(\omega_s) = \mathcal{A} \sum_{n_m=0}^{10} S_{n_m}(\omega_s) + S_{\text{off}}, \quad (34)$$

where \mathcal{A} is a scaling factor, S_{off} is an offset, and $S_{n_m}(\omega_s)$ is the contribution of the qubit spectrum with n_m magnons excited in the uniform magnetostatic mode. The small asymmetry of the qubit spectrum corresponding to $n_m = 0$ is due to the finite photon occupancy of the microwave cavity mode that is used to probe the qubit. The effect of the photon occupation in the probe mode can be considered as follows:

$$S_{n_m}(\omega_s) \approx S_{n_m, n_p=0}(\omega_s) + \mathcal{B} \times S_{n_m, n_p=1}(\omega_s), \quad (35)$$

where $\mathcal{B} = 0.03$ is the relative spectral weight between the one-photon and the zero-photon peaks. To consider the ac Stark shift of the qubit frequency by the photons in the probe mode used to measure the qubit spectrum, the following is substituted as

$$\tilde{\omega}_q \rightarrow \omega_q^{(n_p=0)} = \tilde{\omega}_q + B_p, \quad (36)$$

where $\omega_q^{(n_p=0)}$ is the ac-Stark-shifted qubit frequency with the Kittel mode in the vacuum state. The qubit linewidth with the Kittel mode in the vacuum state is substituted to

$$\gamma_q \rightarrow \gamma_q^{(n_p=0)} = \gamma_q + \kappa_p D_p^{\text{ss}}, \quad (37)$$

where $\gamma_q^{(n_p=0)}$ is the linewidth increased by the measurement-induced dephasing from photons in the probe mode. The parameters fixed in the fit of the qubit spectrum are the qubit frequency $\tilde{\omega}_q$, the qubit linewidth γ_q , the probe mode occupancy \bar{n}_p^g , the qubit-probe-mode dispersive shift χ_{q-p} , the probe cavity-mode linewidth κ_p , the qubit-magnon-mode dispersive shift χ_{q-m} , the magnon linewidth γ_m , and the drive detuning Δ_a .

To consider the uncertainties of the experimentally measured parameters, the chi-square function χ^2 was defined with nuisance parameters α_j as

$$\chi^2 \equiv \sum_{i=0}^n \frac{\tilde{S}_i - \tilde{S}(\omega_s^{(i)}, \gamma_q', \bar{n}_p^{g'}, \chi_{q-p}', \kappa_p', \chi_{q-m}', \gamma_m')}{\sigma_{\tilde{S}_i}} + \sum_{j=0}^5 \alpha_j. \quad (38)$$

TABLE I. Parameters determined in the experiment. The error ranges indicate the 95% confidence interval.

Parameter	Symbol	Value
Dressed magnon frequency	$\omega_m^g/2\pi$	7.94962 GHz
ac-Stark-shifted qubit frequency	$\omega_q^{(n_p=0)}/2\pi$	7.99156 GHz
Broadened qubit linewidth	$\gamma_q^{(n_p=0)}/2\pi$	0.78 ± 0.03 MHz
Probe cavity-mode linewidth	$\kappa_p/2\pi$	3.72 ± 0.03 MHz
Magnon linewidth	$\gamma_m/2\pi$	1.3 ± 0.3 MHz
Qubit-probe-mode dispersive shift	$\chi_{q-p}/2\pi$	-0.8 ± 0.2 MHz
Qubit-magnon-mode dispersive shift	$\chi_{q-m}/2\pi$	1.5 ± 0.1 MHz
Probe-mode occupancy	\bar{n}_p^g	0.22 ± 0.17

with

$$\begin{aligned}
\gamma_q' &= \gamma_q - \alpha_0 \sigma_{\gamma_q}, \\
\bar{n}_p^{g'} &= \bar{n}_p^g - \alpha_1 \sigma_{\bar{n}_p^g}, \\
\chi_{q-p}' &= \chi_{q-p} - \alpha_2 \sigma_{\chi_{q-p}}, \\
\kappa_p' &= \kappa_p - \alpha_3 \sigma_{\kappa_p}, \\
\chi_{q-m}' &= \chi_{q-m} - \alpha_4 \sigma_{\chi_{q-m}}, \\
\gamma_m' &= \gamma_m - \alpha_5 \sigma_{\gamma_m},
\end{aligned}$$

where \tilde{S}_i and $\sigma_{\tilde{S}_i}$ are the average and standard deviation of the experimentally measured spectrum for bin i for a spectroscopy frequency $\omega_s^{(i)}$, respectively. Systematic errors of γ_q , \bar{n}_p^g , χ_{q-p} , κ_p , χ_{q-m} , and γ_m are given by σ_{γ_q} , $\sigma_{\bar{n}_p^g}$, $\sigma_{\chi_{q-p}}$, σ_{κ_p} , $\sigma_{\chi_{q-m}}$, and σ_{γ_m} , respectively.

The results of the fitted data are presented in Fig. 3, where the average number of magnons is fixed to $\bar{n}_m^g = 0$, which is equivalent to $g_{\text{eff}} = 0$. From this, χ^2 was reduced to 167.1/193. This is consistent with the null hypothesis and there was no significant excess in the residuals found for the frequency $\tilde{\omega}_q^{(1)} = \tilde{\omega}_q^{(0)} + 2\chi_{q-m}$. As a result, a 95% confidence level is set for the upper limit of g_{aee} . The upper limit of the average number of magnons \bar{n}_{limit} was calculated as follows:

$$\frac{\int_0^{\bar{n}_{\text{limit}}} L d\bar{n}_m^g}{\int_0^\infty L d\bar{n}_m^g} = 0.95, \quad (39)$$

where L is defined as follows:

$$L \equiv \exp\left(-\frac{\chi^2(\bar{n}_m^g) - \chi_{\text{min}}^2}{2}\right). \quad (40)$$

The chi-square function $\chi^2(\bar{n}_m^g)$ is calculated by varying \bar{n}_m^g , while χ_{min}^2 is the minimum χ^2 . From this, $\bar{n}_{\text{limit}} = 1.1 \times 10^{-2}$ is obtained. The expected residuals calculated with \bar{n}_{limit} is shown in Fig. 3.

The amplitude of the effective magnetic field is given by $B_a \sin \theta$, where θ is the angle between the direction of the external magnetic field \mathbf{B}_0 and the direction of the axion-induced effective magnetic field. From Eqs. (20) and (32), the 95%-confidence-level upper limit on the amplitude of the effective magnetic field at $m_a = 33.123 \mu\text{eV}$ can be determined as follows:

$$B_a \sin \theta < 8.2 \times 10^{-15} \text{ T}. \quad (41)$$

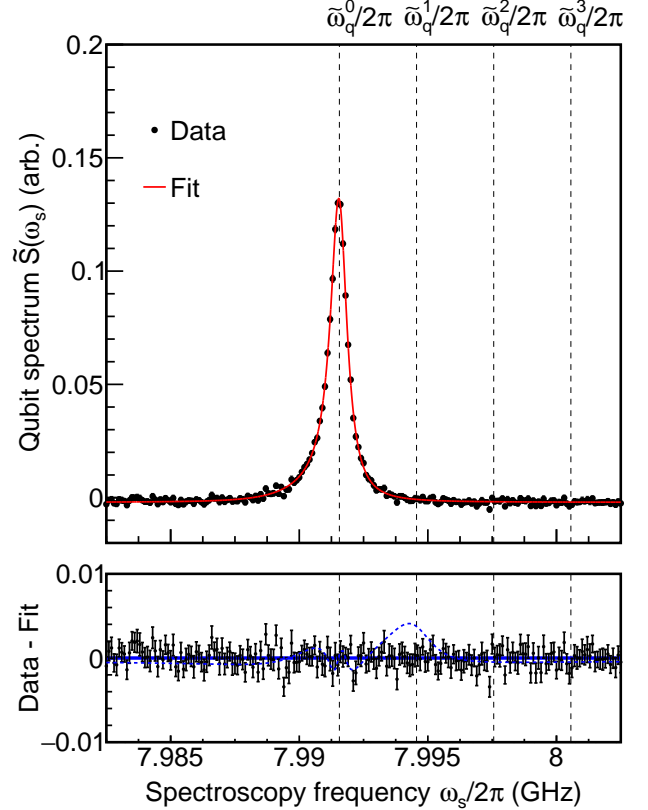


FIG. 3. (a) Measured qubit spectrum $\tilde{S}(\omega_s)$ (black dots) and fit to Eq. (34) (red line). (b) Residuals between the measured qubit spectrum and the fit. The blue dotted curve shows the expected residual at the 95%-confidence-level upper limit ($\bar{n}_m^g = 0.011$) magnified by 10 times.

Using the conventional galactic density of DM, $\rho_{\text{DM}} = 0.45 \text{ GeV/cm}^3$ [43], and the expectation value of the velocity of an axion clump $\langle v_{\text{tot}} \sin \theta \rangle = 338 \text{ km/s}$ (see Appendix A), the upper limit of the axion-electron coupling constant can be obtained:

$$g_{aee} < 1.6 \times 10^{-7}. \quad (42)$$

The axion mass is swept in the range of $33.117 \mu\text{eV} < m_a < 33.130 \mu\text{eV}$ in the above procedure. The constraint

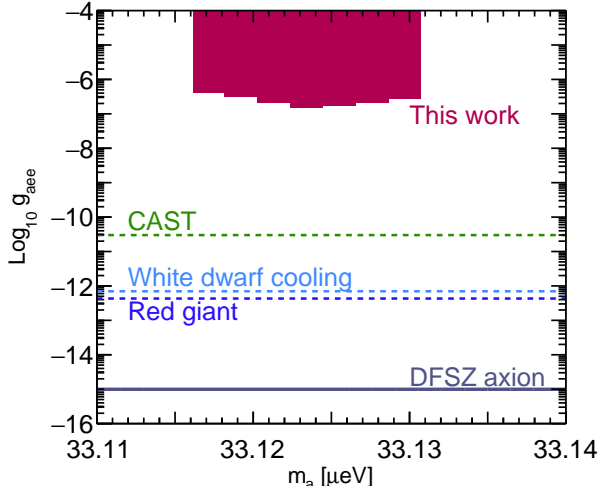


FIG. 4. Constraints on the coupling constant g_{aee} between axions and electrons. The region excluded by this work with 95% confidence is shown in red. The mass range is $33.117 \mu\text{eV} < m_a < 33.130 \mu\text{eV}$. Indirect astrophysical bounds from the solar axion search (CAST experiment [44]), white dwarf cooling [32], and red giants [45] are illustrated with dashed lines. The expected coupling constant for the DFSZ model is represented by a solid line.

is plotted in Fig. 4 and is compared with other previously established bounds on the axion–electron coupling constant.

IV. DISCUSSION

Although this work set the best upper limits for the axion mass $33.117 \mu\text{eV} < m_a < 33.130 \mu\text{eV}$ with the direct axion–electron interaction search, several orders of magnitude improvements are required to reach the theoretical predictions. We discuss some possibilities to improve the sensitivity here. The most straightforward improvement is to increase the statistics with a longer measurement time and optimize the measurement condition. The data used for this axion search was originally taken for a different purpose [28]. The data acquisition time was roughly 4 hours for the spectroscopy window $[7.9825 - 8.0025 \text{ GHz}]$ with a resolution of 100 kHz. Assuming one week data-taking limiting the frequency window to $[7.9860 - 7.9960 \text{ GHz}]$, a relevant window for the measurement of the single-magnon excited state, a 100-fold statistics increase can easily be made. In addition, data acquisition over several days could help to uncover the expected daily and twice-a-day modulations for the axion signal.

Another 100 times statistics increase for a given measurement time can be made by further limiting the spectroscopy window to a few bins which correspond to the magnon linewidth resolution. It should be noted

that this approach requires some improvements on the qubit-magnon coupling condition to narrow the relevant linewidth. With these improvements, it is expected to lower the bound to a coupling strength $g_{aee} \sim 10^{-9}$.

The sensitivity can also be improved by increasing the number of electron spin targets. Coupling N pieces of YIG spheres in the uniform mode to the superconducting qubit increases the effective coupling constant by a factor of \sqrt{N} . The QUAX experiment deployed five pieces of Gallium doped YIG spheres of 1 mm diameter and succeeded in increasing the number of electron spin targets [24]. This technique can also be used for our case and would be expected to improve the sensitivity for the coupling strength.

As aforementioned, Refs. [24–26] showed the upper bound of the axion–electron coupling using the magnon in the spherical ferrimagnetic crystals. Even though this method directly measures the magnon number, the emitted electromagnetic radiation is measured from a microwave cavity where one cavity mode is hybridized with one or multiple uniform magnetostatic modes of ferrimagnetic spheres. Therefore, the background of magnon detection is different. There are still open questions on how to fairly compare this method with the work presented here.

V. CONCLUSION

Magnons can be utilized for exploring the axion DM [24–26] and gravitational waves [46, 47]. In particular, the QND detection of magnons was achieved using a hybrid quantum system consisting of a superconducting qubit and a spherical ferrimagnetic crystal [28]. We applied to the direct axion search based on the axion–electron coupling and analyzed the background data. No significant signal was detected, and an upper limit of the 95% confidence level was set to be $g_{aee} < 1.6 \times 10^{-7}$ for the axion–electron coupling coefficient for the axion mass $33.117 \mu\text{eV} < m_a < 33.130 \mu\text{eV}$. The sensitivity is presently limited by statistics. Increasing the dispersive shift or reducing the power-broadened qubit linewidth and the magnon linewidth will lower the upper bound on the axion–electron coupling.

ACKNOWLEDGEMENT

We would like to thank Yasunobu Nakamura and Dany Lachance-Quirion for providing the data used in this paper. We are also grateful to them for valuable comments. We acknowledge N. Crescini and C. C. Speake for their useful discussions. A.I. was supported by National Center for Theoretical Sciences. J.S. was supported by JSPS KAKENHI Grant Numbers JP17H02894, JP17K18778, and JP20H01902. K.M. was supported by JSPS KAKENHI Grant Numbers 26104005, 16H02189, 19H05806

Appendix A: Velocity of axion clump

The effective magnetic field induced by the axion DM given by Eq. (7) is determined by the velocity of the axion clumps. In this appendix, we show how to estimate it. The relative velocity of an axion clump to the Earth can

be written as

$$\mathbf{v}_{\text{tot}} = v_{\text{solar}}(\sin \alpha, 0, \cos \alpha) + v(\cos \xi, \sin \xi \cos \phi, \sin \xi \sin \phi), \quad (\text{A1})$$

where $v_{\text{solar}} = 220$ km/s [48] is the velocity of the solar system in the Galaxy and α denotes the angle between $\mathbf{v}_{\text{solar}}$ and the external magnetic field B_0 . Here we assumed that the virial velocity in the Galaxy \mathbf{v} has an isotropic Gaussian distribution with a dispersion $\sigma = 270$ km/s. Then, the expectation value of $v_{\text{tot}} \sin \theta$ can be evaluated, where θ is the angle between \mathbf{v}_{tot} and B_0 , as

$$\langle v_{\text{tot}} \sin \theta \rangle = \frac{1}{4\pi} \int_0^{2\pi} d\phi \int_{-1}^1 d(\cos \xi) \frac{4\pi}{(2\pi\sigma^2)^{3/2}} \int_0^\infty dv v^2 e^{-\frac{v^2}{2\sigma^2}} \sqrt{(v_{\text{solar}} \sin \alpha + v \cos \xi)^2 + v^2 \cos^2 \xi \cos^2 \phi}. \quad (\text{A2})$$

For the most conservative case $\alpha = 0$, this results in

$$\langle v_{\text{tot}} \sin \theta \rangle = 338 \text{ km/s}.$$

-
- [1] G. Aad *et al.* (ATLAS Collaboration), *Physics Letters B* **716**, 1 (2012).
 - [2] S. Chatrchyan *et al.* (CMS Collaboration), *Physics Letters B* **716**, 30 (2012).
 - [3] G. Aad *et al.* (ATLAS Collaboration), *Physics Letters B* **726**, 88 (2013).
 - [4] R. J. Crewther, P. Di Vecchia, G. Veneziano, and E. Witten, *Phys. Lett. B* **88**, 123 (1979), [Erratum: *Phys. Lett. B* **91**, 487 (1980)].
 - [5] J. M. Pendlebury *et al.*, *Phys. Rev. D* **92**, 092003 (2015), [arXiv:1509.04411 \[hep-ex\]](#).
 - [6] R. D. Peccei and H. R. Quinn, *Phys. Rev. Lett.* **38**, 1440 (1977).
 - [7] S. Weinberg, *Phys. Rev. Lett.* **40**, 223 (1978).
 - [8] F. Wilczek, *Phys. Rev. Lett.* **40**, 279 (1978).
 - [9] J. Ipser and P. Sikivie, *Phys. Rev. Lett.* **50**, 925 (1983).
 - [10] J. E. Kim, *Phys. Rev. Lett.* **43**, 103 (1979).
 - [11] M. A. Shifman, A. I. Vainshtein, and V. I. Zakharov, *Nucl. Phys. B* **166**, 493 (1980).
 - [12] M. Dine, W. Fischler, and M. Srednicki, *Phys. Lett. B* **104**, 199 (1981).
 - [13] A. R. Zhitnitsky, *Sov. J. Nucl. Phys.* **31**, 260 (1980).
 - [14] M. Dine, W. Fischler, and M. Srednicki, *Physics Letters B* **104**, 199 (1981).
 - [15] P. Sikivie, *Phys. Rev. Lett.* **51**, 1415 (1983).
 - [16] N. Du *et al.* (ADMX Collaboration), *Phys. Rev. Lett.* **120**, 151301 (2018).
 - [17] D. S. Akerib *et al.* (LUX Collaboration), *Phys. Rev. Lett.* **118**, 261301 (2017).
 - [18] K. Abe *et al.*, *Physics Letters B* **724**, 46 (2013).
 - [19] C. Fu *et al.* (PandaX-II Collaboration), *Phys. Rev. Lett.* **119**, 181806 (2017).
 - [20] M. S. Turner, *Physics Reports* **197**, 67 (1990).
 - [21] G. G. Raffelt, *Physics Reports* **198**, 1 (1990).
 - [22] R. Barbieri, M. Cerdonio, G. Fiorentini, and S. Vitale, *Physics Letters B* **226**, 357 (1989).
 - [23] R. Barbieri, C. Braggio, G. Carugno, C. S. Gallo, A. Lombardi, A. Ortolan, R. Pengo, G. Ruoso, and C. C. Speake, *Phys. Dark Univ.* **15**, 135 (2017), [arXiv:1606.02201 \[hep-ph\]](#).
 - [24] N. Crescini, D. Alesini, C. Braggio, G. Carugno, D. D. Gioacchino, C. S. Gallo, U. Gambardella, C. Gatti, G. Iannone, G. Lamanna, C. Ligi, A. Lombardi, A. Ortolan, S. Pagano, R. Pengo, G. Ruoso, C. C. Speake, and L. Taffarello, *The European Physical Journal C* **78**, 703 (2018).
 - [25] G. Flower, J. Bourhill, M. Goryachev, and M. E. Tobar, *Physics of the Dark Universe* **25**, 100306 (2019).
 - [26] N. Crescini, D. Alesini, C. Braggio, G. Carugno, D. D. Agostino, D. D. Gioacchino, P. Falferi, U. Gambardella, C. Gatti, G. Iannone, C. Ligi, A. Lombardi, A. Ortolan, R. Pengo, G. Ruoso, and L. Taffarello, *Phys. Rev. Lett.* **124**, 171801 (2020), [arXiv:2001.08940 \[hep-ex\]](#).
 - [27] S. K. Lamoreaux, K. A. van Bibber, K. W. Lehnert, and G. Carosi, *Phys. Rev. D* **88**, 035020 (2013).
 - [28] D. Lachance-Quirion, Y. Tabuchi, S. Ishino, A. Noguchi, T. Ishikawa, R. Yamazaki, and Y. Nakamura, *Sci. Adv.* **3**, e1603150 (2017).
 - [29] L. Hui, J. P. Ostriker, S. Tremaine, and E. Witten, *Phys. Rev. D* **95**, 043541 (2017).
 - [30] D. J. E. Marsh, *Phys. Rept.* **643**, 1 (2016).
 - [31] A. Aoki and J. Soda, *Int. J. Mod. Phys. D* **26**, 1750063 (2016).
 - [32] A. H. C rsico, A. D. Romero, L. G. Althaus, E. Garc a-Berro, J. Isern, S. Kepler, M. M. M. Bertolami, D. J. Sullivan, and P. Chote, *Journal of Cosmology and Astroparticle Physics* **07** (2016), 036.
 - [33] W. Heisenberg, *Zeitschrift f r Physik* **38**, 411 (1926).
 - [34] T. Holstein and H. Primakoff, *Phys. Rev.* **58**, 1098 (1940).

- [35] C. Kittel, [Phys. Rev. **110**, 1295 \(1958\)](#).
- [36] Y. Nakamura, Y. A. Pashkin, and J. S. Tsai, [Nature **398**, 786 \(1999\)](#).
- [37] Y. Tabuchi, S. Ishino, A. Noguchi, T. Ishikawa, R. Yamazaki, K. Usami, and Y. Nakamura, [Comptes Rendus Physique **17**, 729 \(2016\)](#).
- [38] Y. Tabuchi, S. Ishino, A. Noguchi, T. Ishikawa, R. Yamazaki, K. Usami, and Y. Nakamura, [Science **349**, 405 \(2015\)](#).
- [39] D. Lachance-Quirion, Y. Tabuchi, A. Gloppe, K. Usami, and Y. Nakamura, [Applied Physics Express **12**, 070101 \(2019\)](#).
- [40] D. Lachance-Quirion, S. P. Wolski, Y. Tabuchi, S. Kono, K. Usami, and Y. Nakamura, [Science **367**, 425 \(2020\)](#).
- [41] J. Koch, T. M. Yu, J. Gambetta, A. A. Houck, D. I. Schuster, J. Majer, A. Blais, M. H. Devoret, S. M. Girvin, and R. J. Schoelkopf, [Phys. Rev. A **76**, 042319 \(2007\)](#).
- [42] J. Gambetta, A. Blais, D. I. Schuster, A. Wallraff, L. Frunzio, J. Majer, M. H. Devoret, S. M. Girvin, and R. J. Schoelkopf, [Phys. Rev. A **74**, 042318 \(2006\)](#).
- [43] J. I. Read, [Journal of Physics G: Nuclear and Particle Physics **41**, 063101 \(2014\)](#).
- [44] K. Barth *et al.*, [Journal of Cosmology and Astroparticle Physics **05** \(2013\), 010](#).
- [45] N. Viaux, M. Catelan, P. B. Stetson, G. G. Raffelt, J. Redondo, A. A. R. Valcarce, and A. Weiss, [Phys. Rev. Lett. **111**, 231301 \(2013\)](#).
- [46] A. Ito, T. Ikeda, K. Miuchi, and J. Soda, [Eur. Phys. J. C **80**, 179 \(2020\)](#), [arXiv:1903.04843 \[gr-qc\]](#).
- [47] A. Ito and J. Soda, [Eur. Phys. J. C **80**, 545 \(2020\)](#), [arXiv:2004.04646 \[gr-qc\]](#).
- [48] J. Bovy *et al.*, [Astrophys. J. **759**, 131 \(2012\)](#).